Investigating the effect of Milky Way dwarf spheroidal galaxies extension on dark matter searches with Fermi-LAT data

Mattia Di Mauro,[1,*] Martin Stref,[2,†] and Francesca Calore[2,‡]
[1]*INFN, Torino, Via Pietro Giuria 1, 10125 Torino, Italy*
[2]*LAPTh, USMB, CNRS, F-74940 Annecy, France*

(Received 12 August 2022; accepted 25 November 2022; published 30 December 2022)

Satellite galaxies of the Milky Way with high mass-to-light ratios and little baryon content, i.e., dwarf spheroidal galaxies (dSphs), are among the most promising targets to detect or constrain the nature of dark matter (DM) through its final annihilation products into high-energy photons. Previously, the assumption that DM emission from dSphs is pointlike has been used to set strong constraints on DM candidates using data from the Fermi Large Area Telescope (LAT). However, due to their high DM densities and proximity, dSphs actually have sufficient angular extension to be detected by the Fermi-LAT. Here, we perform a comprehensive analysis about the impact of accounting for angular extension in the search for gamma-ray DM signals toward known dSphs with Fermi-LAT. We show that, depending on the dSph under consideration, limits on the DM cross section can be weakened by up to a factor of 2–2.5, while the impact on the stacked, i.e., combined, limits is at most 1.5–1.8 depending on the annihilation channel. This result is of relevance when comparing dSph limits to other multimessenger DM constraints and for testing the DM interpretation of anomalous "excesses."

DOI: 10.1103/PhysRevD.106.123032

I. INTRODUCTION

Dark matter (DM) represents about the 85% of matter in our Universe [1], and yet its particle nature is a major puzzle for contemporary physics. This puzzle can be tackled from several corners. Among them, indirect searches offer a unique way to probe different aspects of DM through a plethora of astroparticle observables, from cosmic surveys to fluxes of cosmic rays, see e.g., [2,3].

Traditionally, indirect searches look for signatures of cosmic photons and charged particles from GeV to TeV energies produced by DM annihilation or decay in space. Indeed, DM, in the context of weakly interacting massive particles (WIMPs), is believed to annihilate or decay into standard model particles which are not stable but rapidly hadronize and/or decay producing fluxes of stable, observable particles such as photons and cosmic rays (e.g., positrons and antiprotons). Signals of the DM production of cosmic particles are then searched for over the more abundant astrophysical background and foreground emissions. Among the possible cosmic particles, photons have the advantage of direct propagation on galactic scales and DM can be searched in the direction of specific astrophysical objects with predicted high DM density. Several DM searches have been performed in the last 14 years using gamma-ray data of the Fermi Large Area Telescope (LAT) in the direction of different astrophysical targets such as clusters of galaxies, Milky Way dwarf spheroidal galaxies (dSphs hereafter) irregular galaxies, the Milky Way halo, and the Galactic Center, see e.g., [4] for an overview. None of them have been brought to a clear detection, and strong constraints on the DM particle properties have been set.

Perhaps the most promising targets so far used to identify (and/or constrain) the nature of DM are Milky Way dSphs, which are characterized by mass-to-light ratios in the range 10–1000. Moreover, these objects are thought to have very little baryon content and possible astrophysical production of photons, i.e., from pulsars [5] (see [6] for a review). DSphs have been targeted by several instruments, from radio wavelengths to high-energy gamma rays, and have allowed us to set some of the strongest constraints in the annihilation cross section vs mass plane for WIMP DM [7–12]. Nonetheless, in recent years, scientists have highlighted some limitations which weaken the robustness of the DM limits from dSphs. First, statistical and systematic modeling uncertainties of the DM distribution in dSphs (e.g., contamination of foreground nonmember stars and/or triaxiality) are especially important for ultrafaint objects, for which only hundreds of member stars are detected [13]. Uncertainties related to departure from spherical symmetry and velocity anisotropy of the DM halo, as well as the effect of contaminating foreground stars, may significantly alter the predicted DM flux, and affect, in turn, the limits by a factor of 2 to 3 [14–20]. Secondly, systematic uncertainties

*dimauro.mattia@gmail.com
†stref@lapth.cnrs.fr
‡calore@lapth.cnrs.fr

associated with the modeling of the astrophysical background at the dSph position can weaken the limits by a factor of a few, as in the case when assuming purely data-driven methods for background estimations [21–25]. Finally, the contamination from pulsars and millisecond pulsars may be larger than previously believed [26].

Most of the searches for a DM signals toward dSphs have been performed by looking for an excess of photon counts over the modeled astrophysical background matching a pointlike DM signal from the dSph direction (see, e.g., [8–12,24,25]). This was motivated by the fact that the size of the possible DM halos around dSphs is expected to be much smaller than the Fermi-LAT point-spread function (PSF) below 1 GeV. References [7,27,28] investigated the effect of the DM density profile extension in the analysis. However, with several years of Fermi-LAT observations and the improved data selection of Pass 8 [29], the size of extension of sources can be found, for relatively bright sources, to have values as low as 0.1°–0.2°.

Source extension has been studied in the context of searches for subhalos in unidentified Fermi sources [30–34], as well as included in the calculation of sensitivity predictions with future gamma-ray instruments [35,36]. In particular, Refs. [37,38] explicitly showed that, in typical simulations of DM subhalos, there is a correlation between the DM annihilation expected flux—which is proportional to the so-called J factor, the integral along the line of sight (l.o.s.) of the DM density squared—and the halo extension. As noticed therein, this also naturally applies to dSphs, which are the more massive subhalos, i.e., with large J factors, and the smallest objects where star formation has been triggered. Based on that and according to both semianalytical and numerical simulations, DM subhalos, and even more so dSphs, can have an angular extension in the sky larger than the Fermi-LAT sensitivity for extended source detection [31,37]. References [39,40] studied the effect of the source extension on the geometrical factor for irregular galaxies and they found the constraints on a possible DM contribution by including the extension of the DM templates. Therefore, the search for a DM signal in dSphs galaxies can be affected by the likely halo extension.

In this paper, we follow our previous work in [37] and explore, for the first time, the impact of including halo extension on the DM limits using Fermi-LAT data collected from the direction of known dSphs. First, we calculate the expected effect using simulated data showing that the DM halo size indeed affects the upper limits on the annihilation cross section. Then, we demonstrate that the effect found in simulations is confirmed with real data: Depending on the dSph extension and properly accounting for it can weaken the limits by up to a factor of 1.5–1.8, depending on the annihilation channel. This result can impact the DM interpretation of the anomalous Fermi-LAT Galactic Center excess, see e.g., [41] for a review. In fact, the best-fit region for the DM mass and annihilation cross section that fit the GeV excess observations starts to be challenged by different, complementary constraints on DM particle models set with other targets or other messengers. If this tension is confirmed this may be a strong indication that the DM interpretation of this excess should be dismissed. As for dSphs, it has been shown that uncertainties of a factor of a few may worsen or alleviate this tension. As we will show, the fact that including the dSphs extension weakens these limits by a factor up to 1.5–1.8 may therefore be relevant to assess the tension between dSph limits and the DM GeV excess best-fit region. Finally, we also assess what the impact of triaxiality on the final limits is when the full halo extension is considered, similar to what was done in [19].

The paper is organized as follows. In Sec. II, we present the set of dSphs used in the present work and how we model the distribution of DM therein. In Sec. III, we describe the data selection and analysis technique, which we validate on mock data. Validation tests and results are presented in Sec. IV. We finally illustrate our results in Sec. V, and conclude in Sec. VI.

II. DARK MATTER DENSITY IN DWARF SPHEROIDAL GALAXIES

A. Spherical templates

Gamma-ray searches for DM annihilation in dSphs rely on the evaluation of the so-called J factor

$$J(\Delta\Omega) = \int_{\Delta\Omega}\int_{\text{l.o.s.}} \rho^2(l,\Omega)\mathrm{d}l\mathrm{d}\Omega, \tag{1}$$

where l is the l.o.s. coordinate, ρ is the DM density, and $\Delta\Omega$ is the solid angle over which integration is performed. In order to compute this J factor, one needs to model the DM density inside dSphs. This is usually done adopting the Jeans equations and the observed dynamics of stars hosted by these systems. In this work, we rely on the mass modeling performed in two previous studies [10,25], and we consider a sample of 22 dSphs. These can be divided into two broad class: *classical* objects which contain hundreds to thousands of member stars, and *ultrafaint* objects which only possess tens of stars. Among our 22 dSphs, we have 8 classical dSphs and 14 ultrafaint dSphs.

For classical dSphs we rely on Ref. [25], which performed a Jeans analysis assuming spherical symmetry and steady state for each object. The usual degeneracy between density and velocity anisotropy is lifted by considering higher-order Jeans equations [42]. The DM density follows the `coreNFW` functional form introduced in Ref. [43]

$$\rho_{\text{cNFW}}(r) = f^n\rho_{\text{NFW}} + \frac{nf^{n-1}(1-f^2)}{4\pi r^2 r_c}M_{\text{NFW}}, \tag{2}$$

where $f = \tanh(r/r_c)$ and r_c is the core radius. The quantities ρ_{NFW} and M_{NFW} refer to the density and mass of the well-known Navarro-Frenk-White (NFW) profile [44]

TABLE I. Sample of dSphs used in this study with their associated J_{05}, $J_{\rm tot}$, θ_{68}, $\theta_{\rm tot}$ and distance D. DSphs in the top rows are taken from [25], classical dSphs, while dSphs in the bottom rows are taken from Ref. [10], ultrafaint dSphs.

	$\log_{10}(J_{05})$ (GeV^2/cm^5/sr)	$\log_{10}(J_{\rm tot})$ (GeV^2/cm^5/sr)	θ_{68} (deg)	$\theta_{\rm tot}$ (deg)	D (deg)
Ursa Minor	18.31 ± 0.08	18.55 ± 0.05	0.59	0.84	76
Draco	18.64 ± 0.04	18.73 ± 0.03	0.35	0.84	76
Sculptor	18.39 ± 0.05	18.67 ± 0.09	0.65	1.02	86
Sextans	18.07 ± 0.08	18.15 ± 0.06	0.35	0.84	86
Leo I	17.50 ± 0.06	17.52 ± 0.06	0.12	0.31	254
Leo II	17.51 ± 0.05	17.51 ± 0.05	0.07	0.13	233
Carina	17.92 ± 0.07	18.01 ± 0.11	0.36	0.88	105
Fornax	17.76 ± 0.05	18.00 ± 0.07	0.59	0.94	138
Aquarius II	18.26 ± 0.62	18.30 ± 0.67	0.19	5.54	108
Bootes I	18.17 ± 0.30	18.34 ± 0.41	0.52	5.41	66
Canes Ven. I	17.35 ± 0.16	17.39 ± 0.21	0.17	5.90	210
Canes Ven. II	17.84 ± 0.53	17.92 ± 0.60	0.25	7.05	160
Carina II	18.22 ± 0.58	18.34 ± 0.66	0.38	3.21	37
Coma Beren.	19.01 ± 0.38	19.21 ± 0.55	0.58	6.59	42
Hercules	17.30 ± 0.54	17.32 ± 0.57	0.11	3.19	132
Horologium I	18.68 ± 1.02	18.70 ± 1.06	0.13	4.94	87
Reticulum II	18.92 ± 0.41	19.09 ± 0.62	0.51	4.70	32
Segue 1	18.96 ± 0.71	19.00 ± 0.77	0.17	2.84	23
Tucana II	18.83 ± 0.56	19.03 ± 0.63	0.57	6.76	57
Ursa Major I	18.22 ± 0.29	18.28 ± 0.34	0.24	5.85	97
Ursa Major II	19.46 ± 0.41	19.71 ± 0.53	0.74	8.78	35
Willman 1	19.52 ± 0.55	19.59 ± 0.70	0.24	5.68	38

$$\rho_{\rm NFW}(r) = \rho_s \frac{r_s}{r} \frac{1}{(1 + r/r_s)^2}, \tag{3}$$

where ρ_s and r_s are the scale density and scale radius, respectively. While NFW describes a system with a cuspy density profile, `coreNFW` is flexible enough to describe both cored and cuspy systems. The `coreNFW` profile is further modified to account for tidal stripping as done in Ref. [45]

$$\rho_{\rm cNFWt}(r) = \begin{cases} \rho_{\rm cNFW}(r), & r \le r_t, \\ \rho_{\rm cNFW}(r_t)(r/r_t)^{-\delta}, & r > r_t, \end{cases} \tag{4}$$

where r_t is the tidal radius. This final form is referred to as `coreNFWtides`. The DM profile in each dSph is thus characterized by six free parameters: ρ_s, r_s, r_c, n, r_t, and δ. We use the Markov chain Monte Carlo (MCMC) posterior chains provided by Alvarez *et al.* [25] to compute the median value of each parameter and the resulting $J_{05} = J(0.5°)$.[1]

From the same posterior chains, one can compute the fully data-driven probability distribution function (PDF) of the J factor. While stressing the relevance of using these data-driven PDFs, Ref. [25] also checked that a log-normal fit provides a reasonable approximation to the J-factor PDFs for classical dwarfs. Since data-driven J-factor PDFs have not yet been derived for ultrafaint dSphs, for the sake of performing a global and consistent analysis over the sample of classical and ultrafaint dSphs, we have decided to adopt the log-normal approximation of the J-factor PDF for both classical and ultrafaint dSphs.

We quote the J_{05} and corresponding 1-standard-deviation uncertainties from the log-normal fit in the eight top rows of Table I. We also report the total geometrical factor $J_{\rm tot}$ which is integrated up to $5 \times r_{\rm t}$ to account for the DM located beyond $r_{\rm t}$, see Eq. (4), and the corresponding uncertainty.

For ultrafaint dSphs, we refer to Ref. [10]. There, the authors performed a Jeans analysis on a large number of dSphs. Equilibrium and spherical symmetry are also assumed, while the anisotropy is a free constant parameter. The DM profile follows the NFW profile in Eq. (3) thus it is characterized by two free parameters ρ_s and r_s. The profile is sharply truncated at the tidal radius $r_{\rm t}$. Unlike classical dSphs, $r_{\rm t}$ for the ultrafaint dSphs is not directly fitted but instead computed using the formula $r_{\rm t} = [M_{\rm sub}(r_{\rm t})/(2 - {\rm d}\ln M_{\rm host}/{\rm d}\ln R) M_{\rm host}]^{1/3} R$ where R is the radial position of the dSph within the Galaxy and $M_{\rm host}$ is the total mass within that radius. The tidal radius implicitly depends on $\rho_{\rm s}$, $r_{\rm s}$ and the distance D from the dSph which

[1] J_{05} represents the value of the geometrical factor obtained by performing the integration of Eq. (1) as

$$J(\theta_{\rm max}) = 2\pi \int_0^{\theta_{\rm max}} {\rm d}\theta \sin\theta \int_{\rm l.o.s.} \rho^2(l, \Omega) {\rm d}l, \tag{5}$$

where $\theta_{\rm max} = 0.5°$.

is a nuisance parameter of the analysis. We use the publicly available MCMC posterior chains to compute the median value of these parameters. We exclude a number of objects from the analysis of [10]: We remove dSphs which have an unresolved or only partially resolved l.o.s. velocity dispersion. Since we are interested in the impact of extended DM templates, we also remove objects that are not satellites of the Milky Way and are too far away to show any significant extension. In fact, we discard objects with a distance > 300 kpc. We are thus left with 14 dSphs which are listed along with their J_{05} in the 14 bottom rows of Table I. We also report $J_{\rm tot}$ which is integrated up to the tidal radius as a sharp truncation of the profile at $r_{\rm t}$ is assumed for the ultrafaints dSphs. Uncertainties on both J_{05} and $J_{\rm tot}$ are obtained by fitting a log-normal PDF through the corresponding distribution.

Before proceeding to the detailed analysis, we can already single out targets which can be significantly extended. We do this by computing the angle θ_{68} which contains 68% of the total J factor

$$J(\theta_{68}) \equiv 0.68 \times J_{\rm tot}. \tag{6}$$

This angle is computed for each dSph template and the result is shown in the right column of Table I. Very roughly, we expect limits set from objects with $\theta_{68} \gtrsim 0.5°$ to be impacted by the use of an extended template in place of a pointlike one. In particular, Sculptor among the classical dSphs and Ursa Major II among the ultrafaint ones show the largest extensions, 0.65° and 0.74° respectively. Note that for most targets θ_{68} is much smaller than the physical angular extension $\theta_{\rm tot}$ set by the tidal radius.[2] For the usual thermal relic cross section, the DM density near $r_{\rm t}$ is much too low for the annihilation to be detectable so θ_{68} is a better proxy for the detectable extension of an object. Nevertheless, we provide $\theta_{\rm tot}$ and the distance D to the source in Table I. We note that $\theta_{\rm tot}$ is lower for classical dSphs than for ultrafaint dSphs, which can be traced back to lower values of $r_{\rm t}$. We recall that for classical dSphs $r_{\rm t}$ is simply a fitting parameter, which potentially underestimates the true tidal radius. This has no consequence on our analysis since θ_{68} is a more relevant parameter.

As a concluding remark for this section, we would like to point out that the angular size (or $\theta_{68\%}$) is an effective parameter which depends on the fundamental dSph parameters, namely the distance and the DM spatial profile. By virtue of the definition of $\theta_{68\%}$, cuspier profiles produce a smaller $\theta_{68\%}$ be since more flux is contained in a smaller angular size. So, if the DM profile's parameters (and parametrizations) of the dSphs significantly differ from the ones used here, they will predict a different $\theta_{68\%}$ and yield a different impact of the extension on the single dSph DM limits. We stress, that, for the present work we have made use of the latest and, presumably, most robust analyses for the determination of the mass distribution in dSphs. For the sake of completeness, we have reported the median values of the DM density parameters for each dSph in the Appendix.

B. Nonspherical templates

There is observational evidence for nonsphericity of the luminous halo of several dSphs [46–48]. Furthermore, cold DM-only cosmological simulations show that the DM profile of satellite galaxies are in general not spherical but instead mildly triaxial [49,50], although baryonic feedback effects can make these halos more spherical [51,52]. Since departures from spherical symmetry in the dSph DM profiles are known to be an important source of uncertainty when setting constraints on the annihilation cross section [14,16,18,19], we also consider a triaxial template in our analysis. Such a template is created by simply replacing the spherical radius r in Eq. (4) by the ellipsoidal radius:

$$r \to \sqrt{\left(\frac{x}{a}\right)^2 + \left(\frac{y}{b}\right)^2 + \left(\frac{z}{c}\right)^2} \tag{7}$$

where a, b, and c are the axis parameters with $a \geq b \geq c$ and $abc = 1$. We fix the axis ratios to $b/a = 0.8$ and $c/a = 0.6$ which are values close to the ones found in simulations [49,50] and are also used in the triaxial analysis performed by Ref. [14].

We keep the values of the profile parameters ($\rho_{\rm s}$, $r_{\rm s}$, etc.) obtained from the spherical Jeans analysis. This is not entirely consistent as one should instead redo the Jeans analysis on the data starting from the triaxial ansatz instead of the spherical one. Our goal here however is not to provide the most realistic description but rather to gauge the general impact of triaxiality for an extended target. In the following, we consider three extreme configurations corresponding to the l.o.s. being aligned with either the major, second, or minor axis.

III. DATA SELECTION AND ANALYSIS TECHNIQUE

A. Data selection

We perform our analysis with 12 years[3] of Pass 8 Fermi-LAT data with the P8R3 processing. We select SOURCEVETO class events,[4] passing the basic

[2]This is not strictly the case for the `coreNFWtides` template which has a density that goes smoothly to zero at infinity.

[3]Mission Elapsed Time: 239557417–618050000 s.

[4]SOURCEVETO is an event class recently created by the Fermi-LAT Collaboration to maximize the acceptance while minimizing, at the same time, the irreducible cosmic-ray background contamination. In fact, the SOURCEVETO class has the same contamination level of P8R2_ULTRACLEANVETO_V6 class while maintaining the acceptance of the P8R2_CLEAN_V6 class.

quality filter cuts,[5] and their corresponding P8R3_SOURCEVETO_V2 response functions. We choose energies between 0.5 to 1000 GeV and apply a cut to zenith angles $<100°$ in order to exclude contamination from the limb of Earth. We decide to start our analysis from 0.5 GeV because we want to investigate the effect of the extension of dSphs. Including data with energies <0.5 GeV, where the PSF is much larger, would not improve the sensitivity of our results. In fact the angular resolution below 500 MeV is typically larger than 1° while above 1 GeV could be as low as 0.1°. For each target in our analysis, we select a 14×14 deg^2 region of interest (ROI) centered at the dSphs position and choose a pixel size of 0.08 deg. We only consider spherical templates in this section. Uncertainties associated with triaxiality will be discussed in Sec. V C.

B. Analysis technique

The DM search in our sample of dSphs follows the analysis performed in the past by the Fermi-LAT Collaboration on these sources (see, e.g., [7]) or more recently in the direction of the Andromeda and Triangulum galaxies [53]. We provide a general overview and we refer to Refs. [7,53] for a complete description of the analysis technique. We use the public FERMIPY package (version 0.19.0) to perform a binned analysis with eight bins per energy decade. FERMIPY is a PYTHON wrapper of the official FERMITOOLS, for which we use version 1.3.8.

In each of the 22 dSph ROIs, which we analyze independently,[6] we model the total gamma-ray emission as the sum of *background* plus *signal* events. The astrophysical background model is made up of (1) sources as reported in the 10-year Source Catalog (4FGL-DR2)[7] including sources located at most 2° outside our ROI, (2) the latest released interstellar emission model (IEM), namely `gll_iem_v07.fits`,[8] and (3) its corresponding isotropic template `iso_P8R3_SOURCEVETO_V3_v1.txt`. The signal we look for is an additional source at each dSph position. To model the additional source term, we consider two scenarios: (a) the pointlike source case (`PS` hereafter), where the new source has no extension, and (b) the extended case (`Ext` hereafter), where the additional source spatial distribution is fully included in the fit by making use of the extended templates described in Sec. II.

We perform the following analysis steps:

(1) *Optimization of background model in dSPh ROIs.*—A baseline fit is performed on each ROI including sources in the 4FGL-DR2, IEM, and isotropic template. A refinement of the model is run by relocalizing all pointlike sources in the model. We check that the new positions are compatible with the ones reported in the 4FGL-DR2 catalog. Then, we search for new pointlike sources with a test statistic[9] (TS) $TS > 25$ and distance at least 0.5° from the center of the ROI. A final fit is then performed, where all the spectral energy distribution (SED) parameters of the sources, normalization and spectral index of the IEM, and normalization of the isotropic component are free to vary. With this first step we thus have a background model that represents properly the gamma-ray emission in the ROI. In fact, in all the ROIs considered the residuals found by performing a TS map with the background-only model are at most at the level of $\sqrt{TS} \sim 2$–3. These remaining residuals, if located close to the region of interest, could generate a small signal for the detection of the dSphs.

(2) *SED of additional source at dSph position.*—The additional source associated with DM emission at the position of each dSph is added in the center of the ROI either as pointlike source (`PS` case) or as an extended source (`Ext` case). A fit with the background plus signal model is then performed for the two scenarios in each dSph ROI. The SED for the additional sources at the dSph positions is calculated by performing a fit energy bin by energy bin. Specifically, the SED run gives for each energy bin the value of the likelihood as a function of the photon energy flux, $d\Phi_{\rm dSph}/dE$. With the SED information we can thus test every possible spectrum for the source of interest, including the DM one.

(3) *Conversion from source energy flux to DM parameter space.*—The flux of gamma rays produced from DM particle annihilation is

$$\frac{d\Phi_{\rm DM}}{dE} = \frac{1}{4\pi}\frac{\langle\sigma v\rangle}{2M_{\rm DM}^2} J \times \sum_f Br_f \left(\frac{dN_\gamma}{dE}\right)_f \quad (8)$$

where $M_{\rm DM}$ is the DM mass, $\langle\sigma v\rangle$ defines the annihilation cross section times the relative velocity, averaged over the galactic velocity distribution function and J is the geometrical factor. $(dN_\gamma/dE)_f$ is the gamma-ray spectrum from DM annihilation for a specific annihilation channel labeled as f and Br_f is its branching ratio. We take $(dN_\gamma/dE)_f$ from Ref. [55] as implemented in the FERMITOOLS.[10] We

[5]DATA_QUAL > 0 && LAT_CONFIG == 1.

[6]See Ref. [24] for some limitations related to independent ROI fits.

[7]https://arxiv.org/pdf/2005.11208.pdf.

[8]A complete discussion about this new IEM can be found at https://fermi.gsfc.nasa.gov/ssc/data/analysis/software/aux/4fgl/Galactic_Diffuse_Emission_Model_for_the_4FGL_Catalog_Analysis.pdf.

[9]The TS is defined as twice the difference in maximum log-likelihood between the null hypothesis (i.e., no source present) and the test hypothesis: $TS = 2(\log \mathcal{L}_{\rm test} - \log \mathcal{L}_{\rm null})$ [54].

[10]See the following page for a complete description of the DM model: https://fermi.gsfc.nasa.gov/ssc/data/analysis/scitools/source_models.html#DMFitFunction.

comment about the choice of J-factor parameters and the impact on final constraints in Sec. IV. We consider two DM annihilation channels with a branching ratio equal to 1, b-quark and τ-lepton pair annihilation, which correspond to the most extreme behaviors of the DM SED and should bracket the DM spectral uncertainties. We use the SED information obtained in step 2 to calculate, for every annihilation channel, the likelihood as a function of annihilation cross section and DM mass values. We perform this analysis for each individual source in our sample. For a given DM annihilation channel and mass the theoretical DM SED shape is fixed and for different values of the annihilation cross section ($\langle\sigma v\rangle$) we extract the corresponding likelihood from the SED data.

(4) *Extracting the TS for the detection of DM or upper limits for* $\langle\sigma v\rangle$.—For each individual dSph, we therefore obtain the likelihood as a function of DM mass and annihilation cross section. The DM detection TS is found by finding the maximum of the likelihood in the $\langle\sigma v\rangle$ and DM mass ($M_{\rm DM}$) space and comparing it with the likelihood of the null hypothesis, i.e., the one of the optimized ROI fit without DM emission. The upper limits of $\langle\sigma v\rangle$ are instead calculated in the following way. For a fixed DM mass, we take the likelihood profile as a function of $\langle\sigma v\rangle$, $\mathcal{L}(\langle\sigma v\rangle)$. We then can calculate the upper limits for $\langle\sigma v\rangle$ by finding the minimum of $\mathcal{L}(\langle\sigma v\rangle)$ and calculating the $\langle\sigma v\rangle$ that worsens the best-fit likelihood value by $\Delta\mathcal{L} = 2.71/2$,[11] which is associated with the one-sided 95% C.L. upper limits. In finding the TS or the upper limits for $\langle\sigma v\rangle$, we add to the Poissonian term of the likelihood a factor that takes into account the uncertainty on the J factor, assuming a log-normal distribution of this quantity [7]:

$$\mathcal{L}_i(J_i|J_{{\rm dyn},i},\sigma_i) = \frac{1}{\log(10)J_{{\rm dyn},i}\sqrt{2\pi}\sigma_i} \times \exp\left[-\left(\frac{\log_{10}(J_i)-\log_{10}(J_{{\rm dyn},i})}{\sqrt{2}\sigma_i}\right)^2\right], \quad (9)$$

where $J_{{\rm dyn},i}$ is the best fit for the dynamical geometrical factor for the ith dwarf while σ_i is the error in $\log_{10}(J_{{\rm dyn},i})$ space. Instead J_i is the value of the geometrical factor for which the likelihood is calculated.

According to standard practice, we profile over the J-factor uncertainty. This term of $\mathcal{L}$ disfavors values of J_i much different from the observed one weighting it for the corresponding error. We notice that the J-factor parameters for the `PS` case and the `Ext` do not need to match, and indeed we expect them to differ if the source has an extension larger than 0.5°. For each dSph, the parameters of interest are $J^{\rm ps}_{\rm dyn}$, $\sigma^{\rm ps}$, $J^{\rm Ext}_{\rm dyn}$, $\sigma^{\rm Ext}$. We discuss the choice of the parameters' values in Sec. IV.

Finally, we combine the results obtained by summing all dSph likelihoods. The same procedure as the single dSph case is then applied to derive the *stacked TS* and upper limits on the annihilation cross section.

[11]The fluxes for DM are taken to be non-negative in our analysis. Therefore, the $\Delta\chi^2$ or equivalently the $2\Delta\mathcal{L}$ between the test and null hypothesis associated with the 95% C.L. is 2.71.

C. Mock data generation

For the sake of quantifying the impact of extension, we first run the full analysis chain on a set of mock data. We build simulated data based on the optimized background emission model (1) in each dSph ROI, and we create multiple datasets by randomizing the counts in each pixel following the Poisson statistics.

We then run the full analysis pipeline (1–4) on this mock dataset to quantify what is the sensitivity to a putative DM signal at the dSph positions.

IV. VALIDITY TESTS ON SIMULATED DATA

We here present the results of the validity tests performed on simulated data, generated according to the procedure described in Sec. III. We follow the analysis' steps sketched in Sec. III B for both `PS` and `Ext` scenarios. The goals here are to assess how the upper limits on $\langle\sigma v\rangle$ change when varying the J-factor parameters in the likelihood [Eq. (9)], or when assuming an extended template for the DM flux instead of a PS one. To isolate these effects, we consider a case where we have the background model perfectly under control.

We compute the 95% C.L. upper limits on $\langle\sigma v\rangle$ separately for the `PS` and `Ext` cases. In order to disentangle different effects, we consider the following three cases:

(a) `Case 1`: We assume that the geometrical factor average value and error for the `Ext` and `PS` cases are the same: $J^{\rm ps}_{\rm dyn} = J^{\rm Ext}_{\rm dyn} = J_{05}$, and $\sigma^{\rm ps} = \sigma^{\rm Ext} = \sigma_{J_{05}}$, with values as in Table I. We stress that this choice of parameters is nonphysical since the `Ext` and `PS` J factors must have a different normalization by construction. Nonetheless, this case allows us to isolate the impact of the use of an extended template in the analysis.

(b) `Case 2`: We assume a different J-factor average value for the `Ext` and `PS` case, while we keep the same error for the two cases: $J^{\rm ps}_{\rm dyn} = J_{05}$, $J^{\rm Ext}_{\rm dyn} = J_{\rm tot}$, $\sigma^{\rm ps} = \sigma^{\rm Ext} = \sigma_{J_{05}}$. Parameter values as in Table I. This case is performed to test how the results change taking into

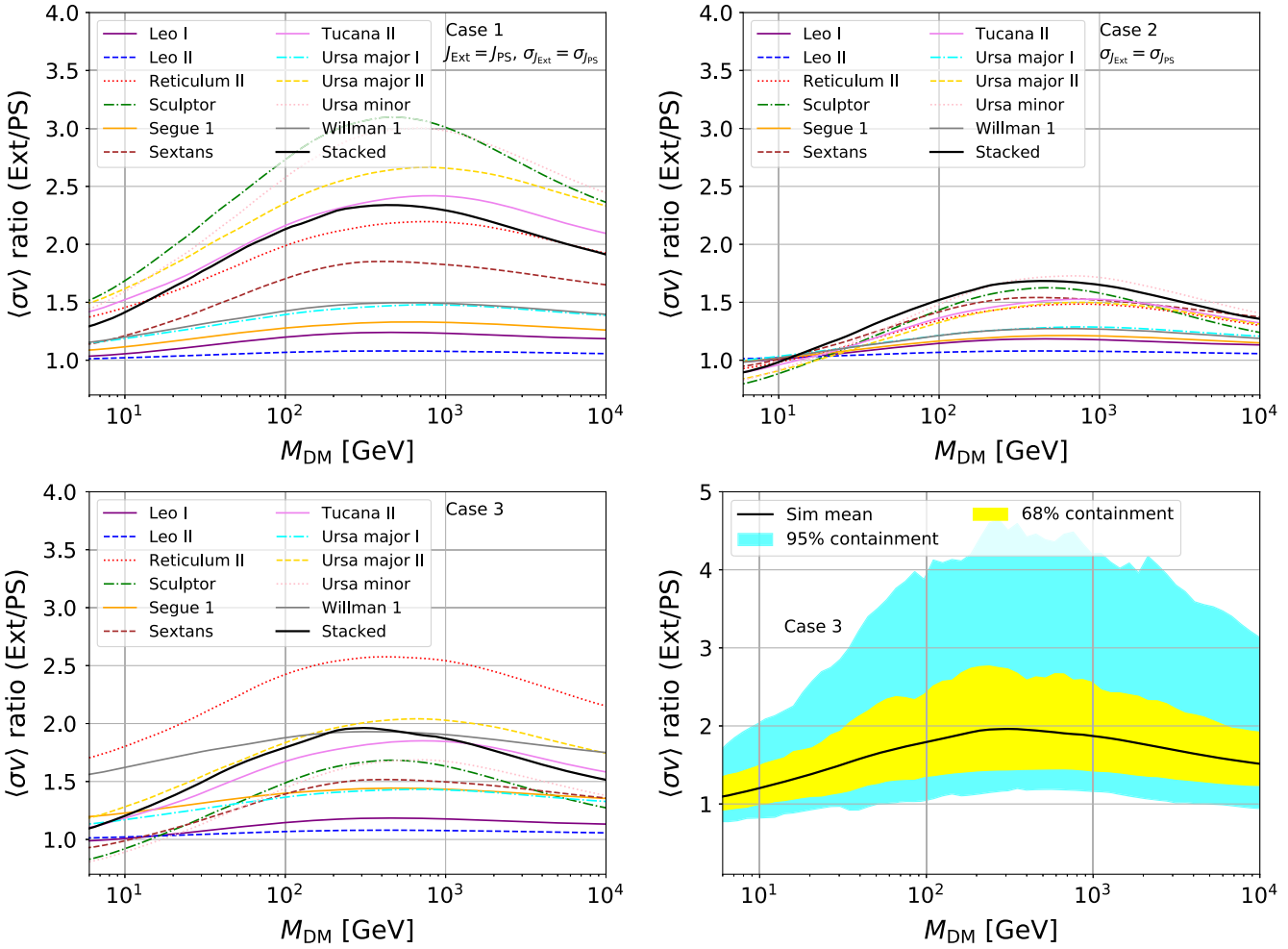

FIG. 1. Simulated data. Ratio of $\langle\sigma v\rangle$ limits Ext/PS for different choices of J-factor parameter values, see description in Sec. IV. Top left: for one half of the dSph sample and total stacked result (black solid line) we show case 1 in the top left panel, case 2 in the top right one, and case 3 in the bottom left one. The stacked result for case 3, together with the corresponding 68% and 95% C.L. bands, is displayed in the bottom right panel.

account both the extended spatial dSph template, as well as the corresponding different J-factor normalization for the Ext and PS models.

(c) Case 3 (baseline): Both the J-factor average and error are different for the Ext and PS cases: $J^{\rm PS}_{\rm dyn} = J_{05}$, $J^{\rm Ext}_{\rm dyn} = J_{\rm tot}$, $\sigma^{\rm PS} = \sigma_{J_{05}}$, and $\sigma^{\rm Ext} = \sigma_{J_{\rm tot}}$. Parameter values are as in Table I. This is the most self-consistent choice of parameters. Indeed, for the PS case, this choice matches the one of previous works [7,10], and can be motivated by the LAT angular resolution. For the Ext case, instead, since the spatial template corresponds to the full DM halo extension, then the most self-consistent choice is to normalize this model with $J_{\rm tot}$.

We show the results obtained in the three cases in Fig. 1 for the parameter $\langle\sigma v\rangle$ ratio Ext/PS for half of our *simulated* dSphs. Similar conclusions are derived by using the other half of the dSph sample. In case 1 (top left), used to isolate the effect of the extended spatial template, we find that the ratio between the cross section in the Ext and PS models is always larger than 1. This implies that the limits in the Ext case are always weaker than the ones in the PS case. For most dSphs, the ratio is between 1.0 and 1.3 at low DM masses, and increases up to 2.0–3.0 for masses between 100 GeV and 1 TeV, as for e.g., Sculptor, Ursa Minor, Fornax, and Ursa Major II.[12] This is explained by the fact that these sources are the most extended ones, see parameter θ_{68} in Table I. The ranking of the sources in the ratio of $\langle\sigma v\rangle$ for Ext and PS models is following exactly the ranking of the parameter θ_{68}. We show this result in Fig. 2, where we report the ratios of the upper limits for $\langle\sigma v\rangle$ obtained for the Ext and PS cases as a

[12]As highlighted above, the effect of the extension on the single dSphs depends on $\theta_{68\%}$, which ultimately depends on the DM profile of the dSphs. So any ranking of dSphs mentioned here has to be understood within the dSph mass modeling adopted in this work.

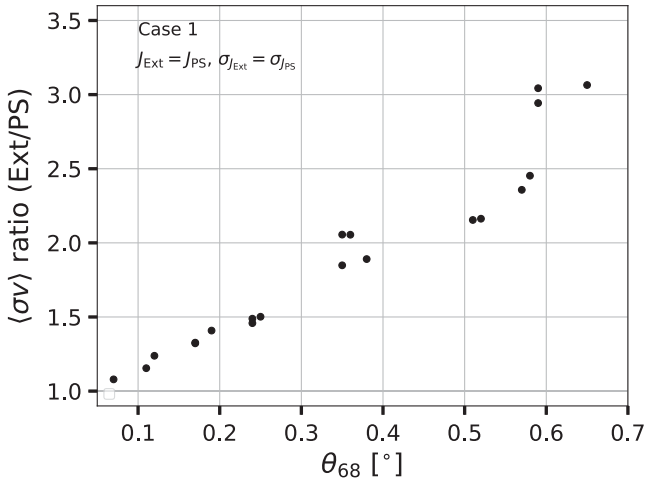

FIG. 2. Ratio of $\langle\sigma v\rangle$ limits for the Ext/PS cases as a function of the parameter θ_{68} as reported in Table I. We show the results obtained for case 1.

function of the parameter θ_{68} (see Table I). A similar mass dependence is found in the stacked analysis shown with a black solid line in Fig. 1. In this case the ratio reaches a maximum of about 2.3 at 400 GeV.

The mass dependence of the ratio can be understood as follows: The Fermi-LAT PSF at low energy is much larger than the one at high energy. Moreover, DM particles with mass below 10 GeV have spectra that peak at low energy where Fermi-LAT has a poor resolution. Therefore, in this mass regime the pointlike source or the extended templates pick up roughly the same flux and, as a consequence, the ratio of the upper limits is expected to be about 1 (or in the other cases to trace the difference between $J_{\rm tot}$ and J_{05}). In particular, the sources for which this ratio is the smallest, very close to 1, are the dSphs with the smallest θ_{68}. At masses of a few hundreds of GeV the DM energy spectra peak at a few tens of GeV where the Fermi-LAT angular resolution is much better. In this case the pointlike source template absorbs less photons than the extended template and in turn the value of $\langle\sigma v\rangle$ for the PS case are smaller than that of the Ext case and the ratio becomes larger than 1. This effect is typically larger for dSphs with a more extended DM template.

In case 2 (top right), where we use the same errors for the geometrical factor but different J-factor average values, the ratio of $\langle\sigma v\rangle$ is driven by a combination of two effects: The different extended template and the different values of J. For DM masses larger than 15 GeV, the limits in the Ext case are always weaker than the ones in the PS case, confirming that the strengthening of the limits at low masses for some dSphs is driven by the $J_{\rm tot}/J_{05}$ ratio. At low masses, $M_{\rm DM} < 15$ GeV, however, the ratio of the cross sections is systematically smaller than 1 for most of the sources. In fact, at such low masses the flux from DM is peaked at very low energy where the Ext and PS models convolved with the very poor PSF appear to have the same extension. Therefore, the ratio of $\langle\sigma v\rangle$ is driven mainly by $J_{\rm tot}/J_{05}$. The sources with the largest θ_{68} are also the ones with the smallest Ext/PS for these values of the DM mass. In this regime the limits on $\langle\sigma v\rangle$ are weaker in the PS case with respect to the Ext approximation. Similarly to what was obtained in case 1, the peak of the $\langle\sigma v\rangle$ ratio is at masses of around 100–1000 GeV and takes maximum values of about 1.3–1.7 for the dSphs that are the most extended.

Finally in case 3 (bottom left), we consider the effect of extension and of the difference in the average and error of the geometrical factors. In this case the general behavior is the same presented before for cases 1 and 2. However, the ranking of the dSphs with the largest $\langle\sigma v\rangle$ ratio between the Ext and PS scenarios is driven mainly by the objects for which the difference of σ_J is the largest, i.e., Reticulum II and Coma Berenices. This is explained by the J-factor likelihood term, Eq. (9), which disfavors values of J_i much different from the observed one. Objects with $\sigma_{J_{\rm tot}}$ much larger than $\sigma_{J_{05}}$, such as Reticulum II, have a likelihood profile that is broader for the Ext with respect to PS scenarios. We can understand this by thinking that the likelihood profile for counts, derived with Poisson statistics, is multiplied by a term related to the geometrical factor see Eq. (1). Therefore, the larger σ_J is in that equation, the broader is the shape of the likelihood as a function of the annihilation cross section, assuming a fixed DM mass. This makes the upper limits found for the former model larger than the one of the latter and, as a result, the ratio Ext/PS is significantly larger than 1. In this case the stacked analysis gives values of the ratio that are at most around 2 for a DM mass of about 300 GeV. In order to demonstrate how the results depend on both θ_{68} and σ_J, we show, in Fig. 3, the ratio of $\langle\sigma v\rangle$ limits for the Ext/PS cases as a function of

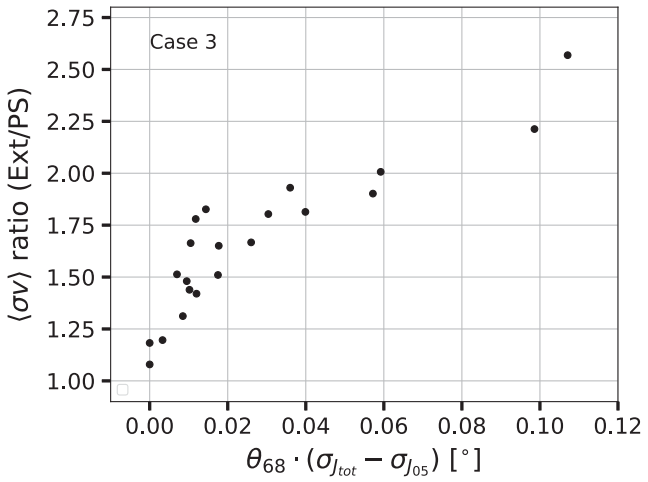

FIG. 3. Ratio of $\langle\sigma v\rangle$ limits for the Ext/PS cases as a function of the parameter $\theta_{68} \cdot (\sigma_{J_{\rm tot}} - \sigma_{J_{05}})$ as reported in Table I. We show the results obtained for case 3.

the combination of parameters $\theta_{68} \cdot (\sigma_{J_{\rm tot}} - \sigma_{J_{05}})$, as reported in Table I. A clear correlation between the upper limits and the quantity $\theta_{68} \cdot (\sigma_{J_{\rm tot}} - \sigma_{J_{05}})$ is present.

It might seem surprising that for objects such as Reticulum II or Coma Berenices the change from $\sigma_{J_{05}}$ to $\sigma_{J_{\rm tot}}$ is much more important than the change in the average observed J factor. We expect the tidal radius $r_{\rm t}$ to be responsible for the change since it is the only parameter that contributes to $J_{\rm tot}$ and not to J_{05}. Indeed, we find that the objects having the largest change in σ_J present two common characteristics: They have a significant extension (θ_{68}) *and* the posterior PDF of the tidal radius $r_{\rm t}$ is broad. Since for the ultrafaint dSphs $r_{\rm t}$ is computed from the fitting parameters $\rho_{\rm s}$, $r_{\rm s}$ and D (see Sec. II), any reduction of the error on these parameters from more accurate data or new analyses would reduce the error on $r_{\rm t}$ and affect the results for `case 3`.

Finally, in the bottom right panel of Fig. 1, we show, for `case 3`, the $\langle \sigma v \rangle$ ratio for the stacked case (red line), together with the 95% and 68% C.L. bands, as obtained for the simulated data.

While in this section we have discussed the effects obtained when isolating the parameter value which distinguish the `Ext` case from the `PS` one, we stress that the `Ext` scenario is fully identified by the self-consistent choice of (a) an extended spatial template, (b) the normalization of the J factor to $J_{\rm tot}$, and (c) the corresponding error on the J factor $\sigma_{J_{\rm tot}}$. In what follows, all results therefore refer to the parameter value choice as in `case 3`.

V. RESULTS WITH REAL DATA

A. Detection significance

We first test the evidence of an additional source template (`PS` or `EXT`) at the position of each dSph in real data, see the description in Sec. III. The TS as a function of DM mass is displayed in Fig. 4 for the case of annihilation into b quarks (top panels) and τ leptons (bottom panels), and for the `PS` (left) and `Ext` (right) source model. We only show the dSphs detected with the highest significance, although this is never significant enough to claim evidence for an excess of photons—the maximal, total TS reached is

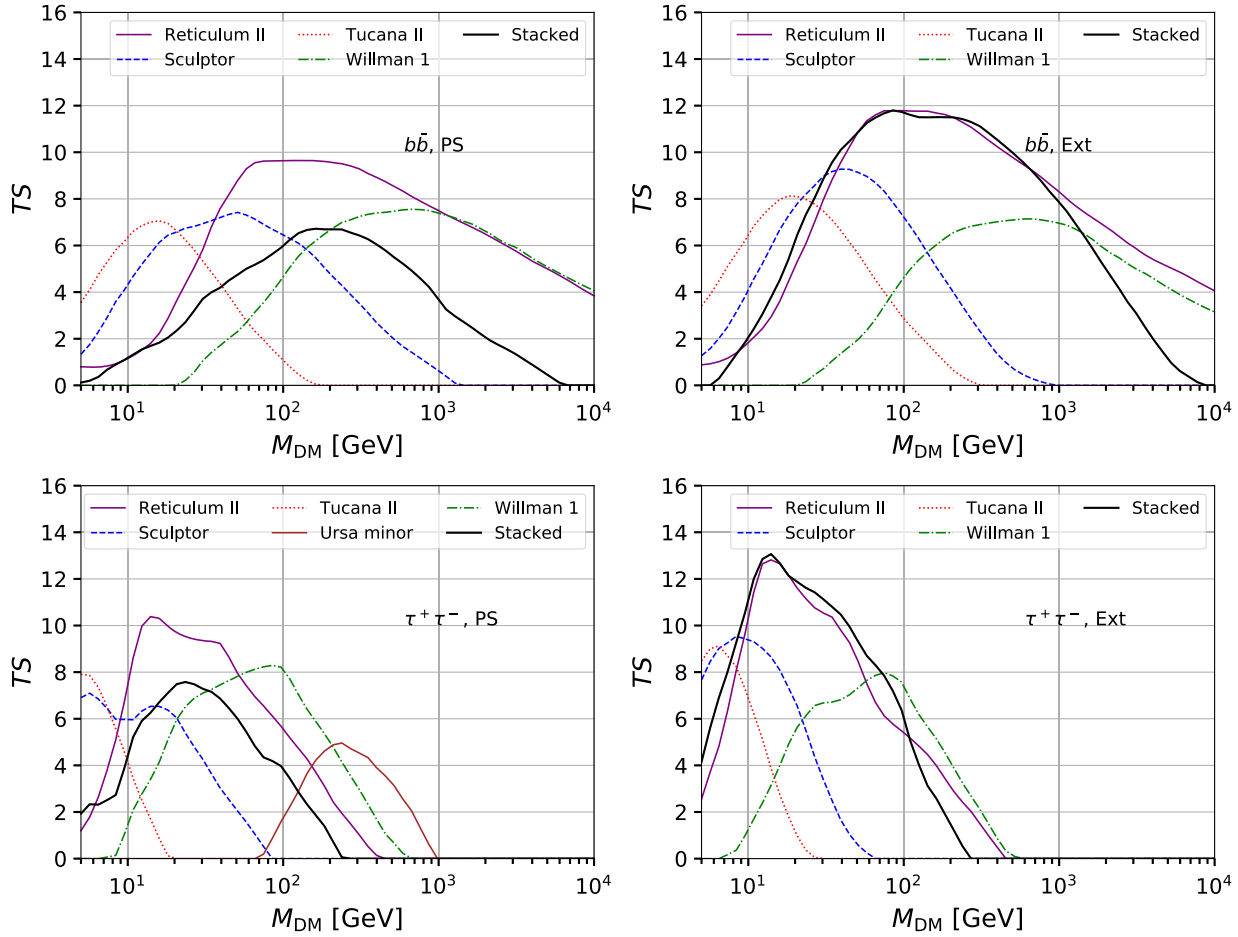

FIG. 4. Real data. Total TS as a function of the DM mass for the dSphs detected with the highest significance. We show the results for $b\bar{b}$ (top panels) and $\tau^+\tau^-$ (bottom panels) annihilation channels and for the `PS` (left panels) and `Ext` scenarios (right panels).

about 13, which roughly corresponds to $\sqrt{13} \sim 3.6\sigma$ local significance (without considering degradation due to trial factors). Among the dSphs selected, the one detected with the highest TS in the Ext scenario is Reticulum II for a DM particle mass of 50–200 (10–20) GeV, $\langle\sigma v\rangle = 1.3 \times 10^{-26}$ (4×10^{-27}) cm^3/s for the $b\bar{b}$ $(\tau^+\tau^-)$ annihilation channel and detected with a $TS \sim 12$ (13), which corresponds to a p-value of 1.2×10^{-3} (7.5×10^{-4}) local, i.e., pretrials, significance of $\sim 3.0\sigma$ (3.1σ),[13] in agreement with previous results, e.g., [56].

We also show in Fig. 4 the TS as a function of DM mass obtained with the combined analysis from all the dSphs in our sample. In case of a real DM signal, we would observe a peak of the TS which is higher than what was found from the individual sources. We find that the maximum TS we obtain, assuming an extended DM template for all dSphs in our sample, is 12 (13) for the $b\bar{b}$ $(\tau^+\tau^-)$ annihilation channel in the Ext case. We find slightly smaller TS values for the PS case. This is consistent with the fact that the extended templates pick up more photons and residuals in the analysis and, as a result, the signal is found with a slightly larger significance.

B. Upper limits on $\langle\sigma v\rangle$

Since the signal detected from each individual dSph and for the stacked sample is not significant, we calculate upper limits for the annihilation cross section, $\langle\sigma v\rangle$. We do so for both the PS and Ext scenarios. Analogously to what was done with simulated data, we show in Fig. 5 the ratio of the limit on $\langle\sigma v\rangle$ using an extended template over the one in the PS limit. We assume DM particles annihilating into $b\bar{b}$ quarks. We display the ratio for single dSphs and for the stacked case, together with the 68% and 95% C.L. bands obtained with the simulations for the null signal. The observed ratios for individual dSphs are mostly contained in the expectation bands. Nonetheless, there are cases where the ratio lies outside the bands. For example the limit ratios found between a DM mass of 300–3000 GeV are slightly below the 95% containment band. This is also the case of Sculptor which, at masses of about 1 TeV, is below the 95% containment band. We stress that the width of the bands here is only indicative and does not include possible effects such as background mismodeling. In fact, we remind the reader that the simulations are performed with mock data assuming a perfect knowledge of the background sources and interstellar emission. Therefore, the fact that some curves are above or below the bands could be due to an imperfect knowledge of the background components in the analysis of real data.

[13]In order to convert the TS into the p-value and the detection significance, we have assumed that the TS distribution of the null hypothesis is equal to the $\chi^2/2$ for 2 degrees of freedom, i.e., the DM mass and annihilation cross section.

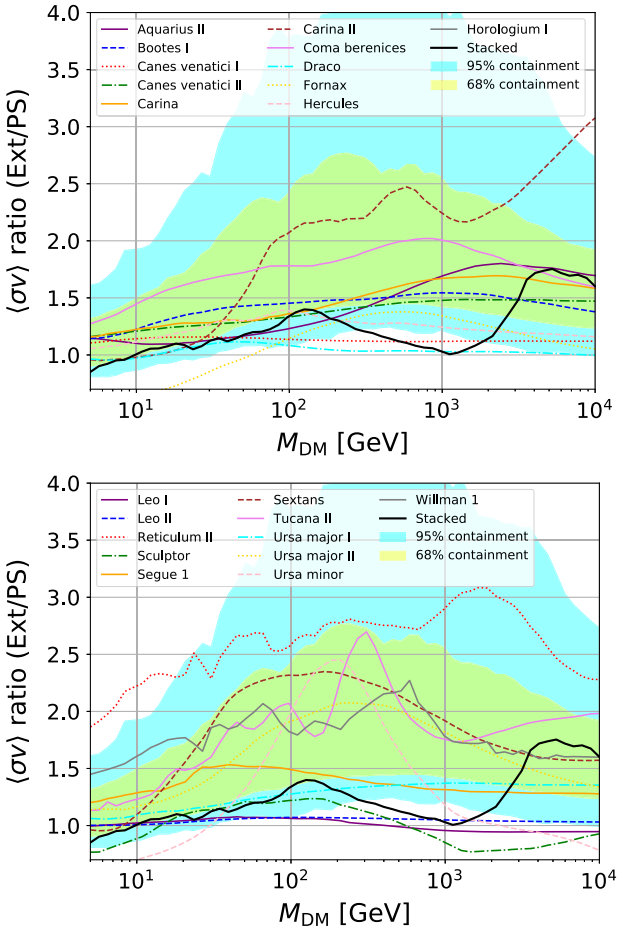

FIG. 5. Real data. Ratio between the 95% C.L. upper limits on $\langle\sigma v\rangle$ found with the extended and pointlike scenarios for the $b\bar{b}$ annihilation channel. We show ratios for all individual dSphs, as well as for the stacked analysis (black line). The bands correspond to the 68%–95% C.L. for the null hypothesis. The top and bottom panels report for legibility purposes two sets of dwarfs in our sample.

In general, with real data analysis, the ratios between the $\langle\sigma v\rangle$ obtained with the Ext template and the one found with the PS case are closer to 1 than what we obtain with simulations, with ratios for single dSphs that reach at most 3 (1.6 for combined limits). However, the result of the real data analysis is compatible with the 95% C.L. containment band derived from simulations. In particular, for DM masses above 20 GeV the ratio between Ext and PS is a factor of about 1.7 smaller with respect to what we obtain for the average of the simulations. The main reason for this result is that the PS case is less compatible with the null hypothesis results than the extended case. In other words, in real data the PS limits are weaker than in simulated data because the small signal detected for the pointlike source case is in real data more significant with respect to the null hypothesis compared to what occurs in the extended scenario. This implies that assuming an extended template for the DM emission makes the limits for $\langle\sigma v\rangle$ more compatible with the null detection.

Finally, we present the limits on $\langle\sigma v\rangle$ as a function of DM mass in Fig. 6 for the $b\bar{b}$ (top panel) and $\tau^+\tau^-$ (bottom panel) annihilation channels for the Ext scenario. We stress that this is the source model that better matches the characteristics of simulated dSphs, and this is therefore the model one has to adopt in order to provide robust and self-consistent constraints from dSphs. The stacked limit derived from the sample of 22 dSphs is represented by the black solid line. The 68% and 95% C.L. containment bands represent the distribution of the limits under the null hypothesis. The upper limits obtained are systematically higher than the 95% containment band obtained with the simulations for $M_{\rm DM} > 25$ GeV for the $b\bar{b}$ channel, and between 10 and 300 GeV for the $\tau^+\tau^-$ channel. The reason for this is related to the presence of small excesses as shown in Fig. 4. The 95% C.L. upper limits are below the thermal cross section [57] up to roughly 10 GeV for both channels. Our results for the upper limits with dSphs are similar at the 20%–30% level with recently published results in Refs. [11,12,24,25] where different list of sources and analysis techniques have been applied. For a more direct comparison, we also show the combined limit when only the eight classical dSphs are considered (green dot-dashed line). We notice that our limits are comparable with [25] for the classical sample although we do not perform a profiling over background uncertainties which can nonetheless impact the limits up to a factor of 3 for high masses (see Fig. 7). Instead, the limits reported recently in Ref. [58] from a combined analysis of Fermi-LAT, HESS, VERITAS, HAWC, and MAGIC data look a factor of about 3 more stringent than ours. This is mainly due to the choice of the geometrical factor values and their uncertainties, and the sample of dSphs considered that differs from ours. We also show, in Fig. 7, the comparison of the upper limits found in this paper compared with the best-fit region for the DM parameters that fit the Galactic Center excess well. We see that the upper limits we find are only slightly above the values of $\langle\sigma v\rangle$ that are compatible with the Galactic Center excess. This demonstrates the importance of properly including the extension in the DM template for dSphs to correctly interpret this excess.

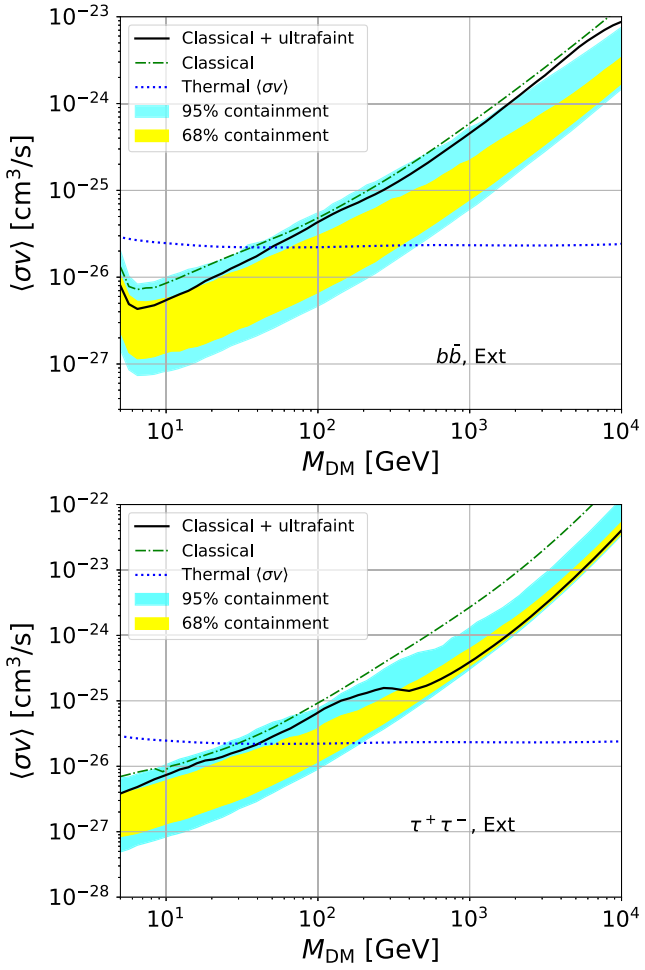

FIG. 6. Real data. 95% C.L. upper limits on the DM annihilation cross section, $\langle\sigma v\rangle$, for annihilation into b quarks (top panel) and τ leptons (bottom panel) in the Ext scenario. The stacked limit derived from the sample of 22 dSphs, classical and ultrafaint, is represented by the black solid line. The 68% and 95% C.L. containment bands represent the distribution of the same limits under the null hypothesis. We also show the combined limit when only the eight classical dSphs are considered (green dot-dashed line). The thermal cross section is taken from [57] (blue dotted).

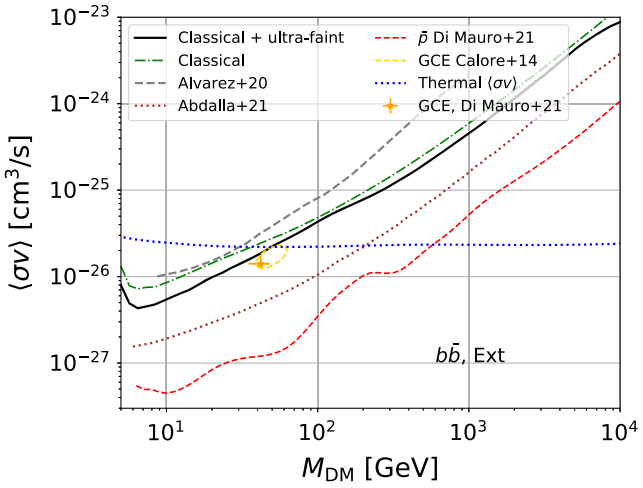

FIG. 7. 95% C.L. upper limits on the DM annihilation cross section, $\langle\sigma v\rangle$, for annihilation into b quarks in the Ext scenario found with our analysis (black solid line). We also show the combined limit when only the eight classical dSphs are considered (green dot-dashed line). The thermal cross section is taken from [57] (blue dotted). As a comparison we report the limits found for classical dSphs in [25] (gray dashed) and the combined limits found for different gamma-ray experiments in [58] (brown dotted). We also overlay antiproton limits [12], and the best-fit 1σ data point for the DM interpretation of the GeV excess taken from Refs. [12,59].

C. Systematic uncertainties from nonspherical templates

We report here the results obtained using the triaxial template introduced in Sec. II B. The analysis is performed for Ursa Minor, which is one of the dSphs most impacted by the use of an extended template in place of a pointlike one. We recall that three specific orientations are considered for the dSph, with the l.o.s. being aligned with either the major, second, or minor axis. The values of the different axes are $a = 1.28$ (major axis), $b = 1.02$ (second axis), and $c = 0.78$ (minor axis). These values for a, b, and c satisfy at the few % level the conditions between b/a, c/a, and abc reported in Sec. II B.

In the first configuration, the halo is less extended because the axes perpendicular to the l.o.s. are the second and minor ones. We also have $\log_{10}(J_{05}) = 18.36$ (in $\mathrm{GeV}^2/\mathrm{cm}^5$) which is 12% higher than the spherical value $\log_{10}(J_{05}) = 18.31$. We recall that the values of the profile parameters (e.g., ρ_s and r_s) are the same for the spherical and triaxial templates. In the second configuration, the major and minor axes are perpendicular to the l.o.s., while $\log_{10}(J_{05}) = 18.3$ is very close to the spherical value. Finally, in the third configuration, the halo is more extended and $\log_{10}(J_{05}) = 18.23$ which is 20% lower than the spherical case. A similar dependence of the J factor on the orientation of the halo and comparable quantitative variations are found in the triaxial analyses of Refs. [14,16].

Ratios between the cross-section exclusion limits obtained with the spherical template and the triaxial one are shown in Fig. 8. The case where the major axis is aligned with the l.o.s. is represented by the dashed-red curve while the second- and minor-axis alignment cases are displayed by the dotted-green curve and blue curve, respectively. We notice that the configuration where the major axis is oriented along the l.o.s. leads to a limit that is very similar to the spherical one (within 5%), while the second axis and minor axis orientations lead to cross-section upper limits that are higher by almost 40% at a DM mass of 100 GeV. This shows that the spatial morphology of the signal impacts the limit, not just the J factor. If the J factor alone was the only relevant parameter, the $\langle\sigma v\rangle$ ratio for major-axis orientation would be smaller than 1, the second-axis orientation would lead to a ratio very close to 1, and the ratio for the minor-axis orientation would be higher. This hierarchy between the different orientations is indeed observed in Fig. 8 but the $\langle\sigma v\rangle$ ratio is shifted upward compared to expectations based on the J factor alone. The ratio is also not flat, and peaks at 100 GeV. The triaxial template thus leads to constraints that are comparable or slightly weaker than the spherical ones. One should keep in mind that the orientations considered here correspond to extreme configurations as there is no reason why one of the main axes should be aligned with the l.o.s. for any given target, thus a 40% weakening of the limit should be seen as a maximal effect of triaxiality. We stress again that our analysis assumes that the DM halo structural parameters are the same in the spherical and triaxial cases. A nonspherical Jeans analysis on the same kinematic data would probably lead to different values for these parameters, which would lead to different J factors. We have shown however that the J factor is not the only source of change and that morphology also plays a role.

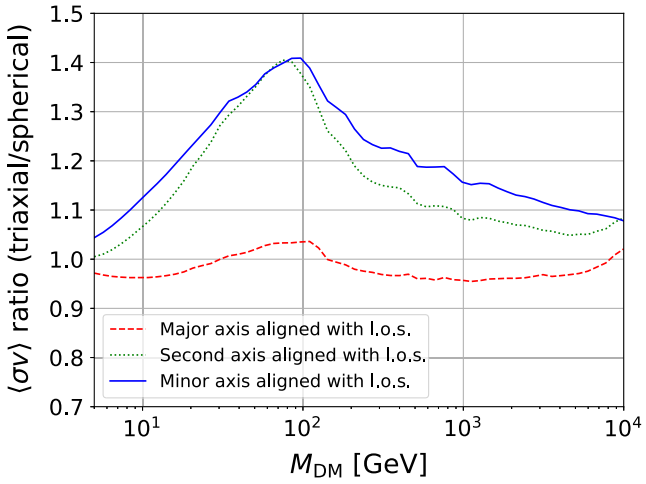

FIG. 8. Ratio between the 95% C.L. upper limits on $\langle\sigma v\rangle$ found with the extended triaxial and extended spherical scenarios for the $b\bar{b}$ annihilation channel for three different orientations of the Ursa Minor DM halo, see text for more details.

VI. CONCLUSIONS

According to the predictions of numerical and semi-analytical simulations, dSphs as the most massive DM subhalos must have a sizable angular extension. In turn, the gamma-ray signal from DM annihilation in these objects is expected not to be pointlike, as typically assumed in the literature, but rather extended in the sky.

In the present work, we first quantified what is the angular extension of a large sample of dSphs using the latest models of the DM distribution in these objects. We found that 8 out of 22 dSphs have an effective angular size larger than the nominal Fermi-LAT angular resolution at a few GeV, which motivated testing the impact of the adoption of an extended spatial template with a thorough gamma-ray data analysis,[14] and eight dSphs in our sample have θ_{68} larger than 0.5°.

The extension, as defined here, is an effective parameter which is ultimately related to the distance and the DM dSph profile. For the same distance, the cuspier the profile is, the smaller the angular extension will be. However, we stress that we relied on state-of-art determination of the dSph mass modeling and DM profile.

[14]The nominal sensitivity of the LAT at GeV energies taken from https://www.slac.stanford.edu/exp/glast/groups/canda/lat_Performance.htm is about 0.5 deg.

We defined a fully self-consistent model for what we called the `Ext` (extended) scenario, which is spherically symmetric, and we quantified the impact of using such a source model against the traditionally adopted pointlike source model, when looking for excess of photons from the dSph directions. We demonstrated that accounting properly for the dSph angular extension has a significant impact on the limits on the DM annihilation cross section. When considering the combined analysis of 22 dSphs, for DM masses larger than 10–15 GeV, the limits weaken by a factor up to 1.5 in the extended case, while for low masses limits with an extended template are compatible with (or slightly stronger than) for the pointlike case. The mass dependence of the ratio can be understood as follows: the Fermi-LAT PSF is much larger at low energies than at high energy. On the other hand, the peak of the gamma-ray flux from DM moves at higher energies when the DM mass increases. Therefore, low-mass DM models are detected with a poorer PSF with respect to high-mass candidates making the `Ext` and `PS` more similar for low-mass values. For the individual dSph analysis, instead, variations up to a factor of 3 less are induced by adopting an extended model for the dSph emission.

Such an effect is similar, in size, to other uncertainties that have been demonstrated in the past to affect (weaken) the robustness of the dSph gamma-ray constraints, either related to the DM distribution in these objects [14–20], or to the (mis)modeling of the astrophysical background at the dSph position [21–25].

We also tested our analysis with a triaxial DM model. We found that the orientation of the axis could weaken the limits by at most a factor of 30%–40% at around 100 GeV.

More generally, our limits are competitive with the ones from other targets such as the Milky Way halo [60–63] and the Galactic Center (see, e.g., [12,64]), while constraints from other messengers such as antiprotons (see, e.g., [12,65]) and from radio wavelengths [66] keep setting the strongest limits on WIMP DM, even if they are typically more subject to astrophysical uncertainties such as the ones related to the cosmic-ray propagation or to the strength of the magnetic field.

Our constraints, as it is for other limits from gamma-ray searches toward dSphs, are only mildly in tension with the DM interpretation of the Fermi GeV excess detected toward the Galactic Center, see e.g., [12,59]. This tension can be alleviated when considering, among others, uncertainties on the galactic DM halo distribution [67,68].

In conclusion, we stress that spatial extension is a common feature of close-by, massive satellites, as shown in [37], and we recommend for the community to take this effect into account when deriving limits from such objects with high-energy photons. As we showed here, the impact of extension is relevant for dSphs. Compared to dSphs, we expect the impact on dark subhalos to be less important, because of the correlation between J factor and extension, but still present. Reference [37] assessed the impact of extension on dark subhalo detection, but we expect an impact also on the limits on DM particle models set through searches for subhalos in unidentified Fermi sources. Finally, we comment that galaxy clusters are also good targets for DM detection and should be rather extended, see the discussions in [69,70]. In the end, the extended analysis of DM targets is undoubtedly of relevance in Fermi-LAT searches, and will be even more so for the next generation gamma-ray telescope, i.e., the Cherenkov Telescope Array [71].

ACKNOWLEDGMENTS

We warmly thank J. Read for providing the MCMC chains from Ref. [25], and A. Pace for helpful discussions regarding Ref. [10]. Mattia Di Mauro research received support from the FELLINI Fellowship for Innovation at INFN, funded by the European Union's Horizon 2020 research program under the Marie Skłodowska-Curie Cofund Action, Grant Agreement No. 754496. We warmly thank Viviana Gammaldi for careful reading of the manuscript and helpful comments. F. C. and M. S. acknowledge support by the Programme National Hautes Énergies (PNHE) through the AO INSU 2019, grant "DMSubG" (PI: F. Calore). Visits of MDM to LAPTh were supported by Université Savoie Mont-Blanc, grant "DISE" (PI: F. Calore). The Fermi-LAT Collaboration acknowledges generous ongoing support from a number of agencies and institutes that have supported both the development and the operation of the LAT as well as scientific data analysis. These include the National Aeronautics and Space Administration and the Department of Energy in the United States, the Commissariatá l'Energie Atomique and the Centre National de la Recherche Scientifique/Institut National de Physique Nucléaire et de Physique des Particules in France, the Agenzia Spaziale Italiana and the Istituto Nazionale di Fisica Nucleare in Italy, the Ministry of Education, Culture, Sports, Science and Technology (MEXT), High Energy Accelerator Research Organization (KEK) and Japan Aerospace Exploration Agency (JAXA) in Japan, and the K. A. Wallenberg Foundation, the Swedish Research Council, and the Swedish National Space Board in Sweden. Additional support for science analysis during the operations phase is gratefully acknowledged from the Istituto Nazionale di Astrofisica in Italy and the Centre National d'Etudes Spatiales in France. This work was performed in part under DOE Contract No. DE-AC02-76SF00515.

APPENDIX: DENSITY PROFILE PARAMETERS

In this section we report a Table II that contains the properties of the dSphs selected in our sample. In particular we list the values of the parameters of the DM density distribution.

TABLE II. Sample of dSphs used in this study with the median value of their associated density profile parameters. DSphs in the top rows are taken from [25], classical dSphs, while dSphs in the bottom rows are taken from Ref. [10], ultrafaint dSphs.

	$\log_{10}(\rho_s)$ ($M_\odot/\mathrm{kpc}^3$)	r_s (kpc)	r_c (kpc)	n	δ	r_t (kpc)
Ursa Minor	7.305	2.169	1.398	0.7852	4.289	1.113
Draco	7.341	1.678	0.1943	0.5389	4.159	1.114
Sculptor	7.360	2.136	1.370	0.7730	4.261	1.534
Sextans	7.408	1.134	0.5343	0.5857	4.218	1.257
Leo I	7.355	1.483	0.4084	0.5209	4.257	1.374
Leo II	7.614	0.9740	0.2283	0.5083	4.212	0.5436
Carina	7.160	1.655	0.5988	0.5263	4.215	1.609
Fornax	7.071	2.750	1.940	0.8600	4.395	2.272
Aquarius II	7.546	1.007	⋯	⋯	⋯	10.41
Bootes I	7.003	1.721	⋯	⋯	⋯	6.212
Canes Ven. I	7.016	1.752	⋯	⋯	⋯	21.56
Canes Ven. II	7.068	2.024	⋯	⋯	⋯	19.61
Carina II	7.321	0.7256	⋯	⋯	⋯	2.097
Coma Beren.	7.457	1.239	⋯	⋯	⋯	4.818
Hercules	7.387	0.6921	⋯	⋯	⋯	7.340
Horologium I	8.029	0.5642	⋯	⋯	⋯	7.459
Reticulum II	7.545	0.8264	⋯	⋯	⋯	2.621
Segue 1	8.302	0.1921	⋯	⋯	⋯	1.139
Tucana II	7.313	1.648	⋯	⋯	⋯	6.741
Ursa Major I	7.425	1.115	⋯	⋯	⋯	9.910
Ursa Major II	7.614	1.250	⋯	⋯	⋯	5.291
Willman 1	8.251	0.4534	⋯	⋯	⋯	3.736

[1] N. Aghanim *et al.* (Planck Collaboration), Astron. Astrophys. **641**, A6 (2020); **652**, C4(E) (2021).
[2] J. M. Gaskins, Contemp. Phys. **57**, 496 (2016).
[3] R. Alves Batista *et al.*, arXiv:2110.10074.
[4] E. Charles *et al.* (Fermi-LAT Collaboration), Phys. Rep. **636**, 1 (2016).
[5] M. Winter, G. Zaharijas, K. Bechtol, and J. Vandenbroucke, Astrophys. J. Lett. **832**, L6 (2016).
[6] L. E. Strigari, Rep. Prog. Phys. **81**, 056901 (2018).
[7] M. Ackermann *et al.* (Fermi-LAT Collaboration), Phys. Rev. Lett. **115**, 231301 (2015).
[8] M. L. Ahnen *et al.* (MAGIC and Fermi-LAT Collaborations), J. Cosmol. Astropart. Phys. 02 (2016) 039.
[9] A. Albert *et al.* (Fermi-LAT and DES Collaborations), Astrophys. J. **834**, 110 (2017).
[10] A. B. Pace and L. E. Strigari, Mon. Not. R. Astron. Soc. **482**, 3480 (2019).
[11] S. Hoof, A. Geringer-Sameth, and R. Trotta, J. Cosmol. Astropart. Phys. 02 (2020) 012.
[12] M. Di Mauro and M. W. Winkler, Phys. Rev. D **103**, 123005 (2021).
[13] V. Bonnivard *et al.*, Mon. Not. R. Astron. Soc. **453**, 849 (2015).
[14] V. Bonnivard, C. Combet, D. Maurin, and M. G. Walker, Mon. Not. R. Astron. Soc. **446**, 3002 (2015).
[15] P. Ullio and M. Valli, J. Cosmol. Astropart. Phys. 07 (2016) 025.
[16] J. L. Sanders, N. W. Evans, A. Geringer-Sameth, and W. Dehnen, Phys. Rev. D **94**, 063521 (2016).
[17] V. Bonnivard, D. Maurin, and M. G. Walker, Mon. Not. R. Astron. Soc. **462**, 223 (2016).
[18] K. Hayashi, K. Ichikawa, S. Matsumoto, M. Ibe, M. N. Ishigaki, and H. Sugai, Mon. Not. R. Astron. Soc. **461**, 2914 (2016).

[19] N. Klop, F. Zandanel, K. Hayashi, and S. Ando, Phys. Rev. D **95**, 123012 (2017).
[20] K. Ichikawa, M. N. Ishigaki, S. Matsumoto, M. Ibe, H. Sugai, K. Hayashi, and S.-i. Horigome, Mon. Not. R. Astron. Soc. **468**, 2884 (2017).
[21] M. N. Mazziotta, F. Loparco, F. de Palma, and N. Giglietto, Astropart. Phys. **37**, 26 (2012).
[22] A. Geringer-Sameth, S. M. Koushiappas, and M. G. Walker, Phys. Rev. D **91**, 083535 (2015).
[23] K. K. Boddy, J. Kumar, D. Marfatia, and P. Sandick, Phys. Rev. D **97**, 095031 (2018).
[24] F. Calore, P. D. Serpico, and B. Zaldivar, J. Cosmol. Astropart. Phys. 10 (2018) 029.
[25] A. Alvarez, F. Calore, A. Genina, J. Read, P. D. Serpico, and B. Zaldivar, J. Cosmol. Astropart. Phys. 09 (2020) 004.
[26] R. M. Crocker, O. Macias, D. Mackey, M. R. Krumholz, S. Ando, S. Horiuchi, M. G. Baring, C. Gordon, T. Venville, A. R. Duffy, R.-Z. Yang, F. Aharonian, J. A. Hinton, D. Song, A. J. Ruiter, and M. D. Filipović, Nat. Astron. **6**, 1317 (2022).
[27] M. Ackermann *et al.* (Fermi-LAT Collaboration), Phys. Rev. D **89**, **042001** (2014).
[28] A. Geringer-Sameth, S. M. Koushiappas, and M. G. Walker, Phys. Rev. D **91**, 083535 (2015).
[29] P. Bruel, T. H. Burnett, S. W. Digel, G. Johannesson, N. Omodei, and M. Wood, arXiv:1810.11394.
[30] B. Bertoni, D. Hooper, and T. Linden, J. Cosmol. Astropart. Phys. 05 (2016) 049.
[31] J. Coronado-Blázquez, M. A. Sánchez-Conde, M. Di Mauro, A. Aguirre-Santaella, I. Ciucă, A. Domínguez, D. Kawata, and N. Mirabal, J. Cosmol. Astropart. Phys. 11 (2019) 045.
[32] H.-S. Zechlin and D. Horns, J. Cosmol. Astropart. Phys. 11 (2012) 050.
[33] M. Ackermann *et al.* (Fermi-LAT Collaboration), Astrophys. J. Suppl. Ser. **237**, 32 (2018).
[34] I. Ciucă, D. Kawata, S. Ando, F. Calore, J. I. Read, and C. Mateu, Mon. Not. R. Astron. Soc. **480**, 2284 (2018).
[35] A. Egorov, A. Galper, N. Topchiev, A. Leonov, S. Suchkov, M. Kheymits, and Y. T. Yurkin, Phys. At. Nucl. **81**, 373 (2018).
[36] T.-L. Chou, D. Tanoglidis, and D. Hooper, Phys. Dark Universe **21**, 1 (2018).
[37] M. Di Mauro, M. Stref, and F. Calore, Phys. Rev. D **102**, 103010 (2020).
[38] J. Coronado-Blázquez, M. A. Sánchez-Conde, J. Pérez-Romero, and A. Aguirre-Santaella (Fermi-LAT Collaboration), Phys. Rev. D **105**, 083006 (2022).
[39] V. Gammaldi, E. Karukes, and P. Salucci, Phys. Rev. D **98**, 083008 (2018).
[40] V. Gammaldi, J. Pérez-Romero, J. Coronado-Blázquez, M. Di Mauro, E. Karukes, M. A. Sánchez-Conde, and P. Saluccix (Fermi-LAT Collaboration), Proc. Sci., ICRC2021 (**2021**) 509.
[41] S. Murgia, Annu. Rev. Nucl. Part. Sci. **70**, 455 (2020).
[42] J. I. Read and P. Steger, Mon. Not. R. Astron. Soc. **471**, 4541 (2017).
[43] J. I. Read, O. Agertz, and M. L. M. Collins, Mon. Not. R. Astron. Soc. **459**, 2573 (2016).
[44] J. F. Navarro, C. S. Frenk, and S. D. M. White, Astrophys. J. **462**, 563 (1996).
[45] J. Read, M. Walker, and P. Steger, Mon. Not. R. Astron. Soc. **481**, 860 (2018).
[46] A. W. McConnachie, Astron. J. **144**, 4 (2012).
[47] M. Walker, in *Planets, Stars and Stellar Systems, Vol. 5: Galactic Structure and Stellar Populations*, edited by T. D. Oswalt and G. Gilmore (Springer, New York, 2013), p. 1039.
[48] R. Sánchez-Janssen *et al.*, Astrophys. J. **820**, 69 (2016).
[49] M. Kuhlen, J. Diemand, and P. Madau, Astrophys. J. **671**, 1135 (2007).
[50] C. A. Vera-Ciro, L. V. Sales, A. Helmi, and J. F. Navarro, Mon. Not. R. Astron. Soc. **439**, 2863 (2014).
[51] M. G. Abadi, J. F. Navarro, M. Fardal, A. Babul, and M. Steinmetz, Mon. Not. R. Astron. Soc. **407**, 435 (2010).
[52] M. Zemp, O. Y. Gnedin, N. Y. Gnedin, and A. V. Kravtsov, Astrophys. J. **748**, 54 (2012).
[53] M. Di Mauro, X. Hou, C. Eckner, G. Zaharijas, and E. Charles, Phys. Rev. D **99**, 123027 (2019).
[54] J. R. Mattox *et al.*, Astrophys. J. **461**, 396 (1996).
[55] T. E. Jeltema and S. Profumo, J. Cosmol. Astropart. Phys. 11 (2008) 003.
[56] D. Hooper and T. Linden, J. Cosmol. Astropart. Phys. 09 (2015) 016.
[57] G. Steigman, B. Dasgupta, and J. F. Beacom, Phys. Rev. D **86**, 023506 (2012).
[58] H. Abdalla *et al.* (Hess, HAWC, VERITAS, MAGIC, H.E.S.S., and Fermi-LAT Collaborations), Proc. Sci., ICRC2021 (**2021**) 528.
[59] F. Calore, I. Cholis, C. McCabe, and C. Weniger, Phys. Rev. D **91**, 063003 (2015).
[60] M. Ackermann *et al.*, Astrophys. J. **761**, 91 (2012).
[61] X. Huang, T. Enßlin, and M. Selig, J. Cosmol. Astropart. Phys. 04 (2016) 030.
[62] H.-S. Zechlin, S. Manconi, and F. Donato, Phys. Rev. D **98**, 083022 (2018).
[63] L. J. Chang, M. Lisanti, and S. Mishra-Sharma, Phys. Rev. D **98**, 123004 (2018).
[64] M. Ackermann *et al.* (Fermi-LAT Collaboration), Astrophys. J. **840**, 43 (2017).
[65] F. Calore, M. Cirelli, L. Derome, Y. Genolini, D. Maurin, P. Salati, and P. D. Serpico, SciPost Phys. **12**, 163 (2022).
[66] M. Regis *et al.*, J. Cosmol. Astropart. Phys. 11 (2021) 046.
[67] M. Benito, N. Bernal, N. Bozorgnia, F. Calore, and F. Iocco, J. Cosmol. Astropart. Phys. 02 (2017) 007; 06 (2018) E01.
[68] M. Benito, A. Cuoco, and F. Iocco, J. Cosmol. Astropart. Phys. 03 (2019) 033.
[69] S. Ando and D. Nagai, J. Cosmol. Astropart. Phys. 07 (2012) 017.
[70] T. Lacroix, G. Facchinetti, J. Pérez-Romero, M. Stref, J. Lavalle, D. Maurin, and M. A. Sánchez-Conde, J. Cosmol. Astropart. Phys. 10 (2022) 021.
[71] B. S. Acharya *et al.* (CTA Consortium Collaboration), *Science with the Cherenkov Telescope Array* (World Scientific, Singapore, 2018).